

Experimental study of quantum coherence decomposition and trade-off relations in a tripartite system

Zhe Ding,^{1,2,*} Ran Liu,^{1,2,*} Chandrashekar Radhakrishnan,^{3,4,5,*} Wenchao Ma,⁶ Xinhua Peng,^{1,2,7} Ya Wang,^{2,7} Tim Byrnes,^{8,9,5,10,11,†} Fazhan Shi,^{1,2,7,‡} and Jiangfeng Du^{1,2,7,§}

¹*Hefei National Laboratory for Physical Sciences at the Microscale and Department of Modern Physics, University of Science and Technology of China, Hefei, 230026, China*

²*CAS Key Laboratory of Microscale Magnetic Resonance, University of Science and Technology of China, Hefei, 230026, China*

³*Laboratoire ESIEA Numérique et Société, ESIEA, 9 Rue Vesale, Paris 75005, France*

⁴*New York University, 1555 Century Avenue, Pudong, Shanghai 200122, China*

⁵*NYU-ECNU Institute of Physics at NYU Shanghai, 3663 Zhongshan Road North, Shanghai 200062, China*

⁶*Department of Chemistry, Massachusetts Institute of Technology, Cambridge, Massachusetts 02139, USA*

⁷*Synergetic Innovation Center of Quantum Information and Quantum Physics, University of Science and Technology of China, Hefei, 230026, China*

⁸*New York University Shanghai, 1555 Century Ave, Pudong, Shanghai 200122, China*

⁹*State Key Laboratory of Precision Spectroscopy, School of Physical and Material Sciences, East China Normal University, Shanghai 200062, China*

¹⁰*National Institute of Informatics, 2-1-2 Hitotsubashi, Chiyoda-ku, Tokyo 101-8430, Japan*

¹¹*Department of Physics, New York University, New York, NY 10003, USA*

Quantum coherence is the most fundamental of all quantum quantifiers, underlying other well-known quantities such as entanglement, quantum discord, and Bell correlations. It can be distributed in a multipartite system in various ways — for example, in a bipartite system it can exist within subsystems (local coherence) or collectively between the subsystems (global coherence), and exhibits a trade-off relation. In quantum systems with more than two subsystems, there are more trade-off relations, due to the various decomposition ways of the coherence. In this paper, we experimentally verify these coherence trade-off relations in adiabatically evolved quantum systems using a spin system by changing the state from a product state to a tripartite entangled state. We study the full set of coherence trade-off relations between the original state, the bipartite product state, the tripartite product state, and the decohered product state. We also experimentally verify the monogamy inequality and show that both the quantum systems are polygamous except for the initial product state. We find that despite the different types of states involved, the properties of the state in terms of coherence and monogamy are equivalent. This illustrates the utility of using coherence as a characterization tool for quantum states.

Introduction.— Quantum coherence has been the focus of investigation in numerous fields such as quantum optics where the fundamental nature of coherence has been investigated using phase-space distributions and higher order correlation functions [1–3]. It was quantified recently in a quantum-information theoretic way [4] and the modern view is that it is the broadest quantum properties and is at the root of various quantum quantifiers such as discord, entanglement, EPR steering, and Bell correlations [5, 6]. A set of axioms were formally introduced which need to be satisfied by a coherence quantifier [4]. This gave rise to the field of resource theories of quantum coherence [7–10], along with an explosion of interest in measurement of coherence [11–15] and its applications [16–19].

Quantum coherence has some unique features not present in other quantifiers such as entanglement and quantum discord (for a review see [9]). One feature is that coherence is a basis dependent property and hence the amount of coherence depends upon the chosen measurement basis. Additionally, coherence can localize in a unipartite system as quantum superposition, or be

present as correlations between different qubits[12]. For example, in a bipartite entangled state $(|00\rangle + |11\rangle)/\sqrt{2}$, the coherence is delocalized and cannot be attributed to any particular qubit. On the other hand, in a separable state $|+\rangle = (|0\rangle + |1\rangle)(|0\rangle + |1\rangle)/2$, the coherence is localized within the qubits. In fact, a maximally entangled state has only global coherence and no local coherence; meanwhile product states are the opposite. This example illustrates the presence of a trade-off between the local and the global coherence in a quantum system. This trade-off is the simplest case and highlights the different complementary distributions of coherence in two qubits. In a multipartite system there are more possible distributions of coherence and hence other types of trade-off relations.

In this Letter, we use a spin system to experimentally measure coherence and investigate the trade-off relations in tripartite systems. We consider two different classes of quantum systems with two and three-body interactions. The quantum coherence is measured at different stages of an adiabatic evolution and various trade-off relations are verified. An example of this process is shown in Fig.

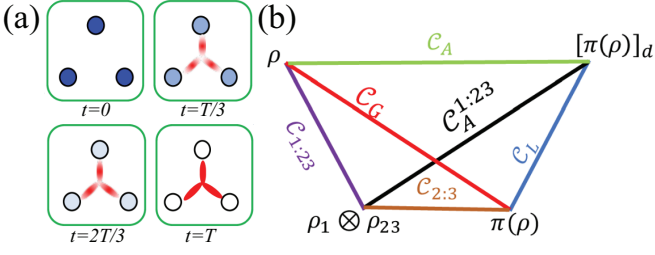


FIG. 1. (a) Quantum coherence trade-off is described in tripartite systems with circles representing the qubits. The blue discs and red leaves represent the local coherence C_L and the global coherence C_G . The strength of the color indicates the strength of the coherence. (b) A geometric picture of different coherences. Coherences are shown as distances between two different density matrices. ρ is the original density matrix; $\pi(\rho)$ and $[\pi(\rho)]_d$ are as described in (5); $\rho_1 = \text{tr}_{2,3} \rho$ and $\rho_{23} = \text{tr}_1 \rho$ are the reduced density matrices.

1(a), where initially the coherence is completely localized within the qubits. Then, when the system is adiabatically evolved, it has both local and global coherence. At the end of the adiabatic evolution, the system has only global coherence. In addition to verifying the trade-off relations and coherence distributions, we analyze the monogamy of coherence. Monogamy, first introduced in the context of entanglement [20, 21], implies that, when Alice and Bob are maximally entangled, they are impossible to be simultaneously entangled with a third party Charlie. This concept was later extended to quantum correlation [22, 23] and quantum coherence [12]. We show that using the various coherence quantifiers and monogamy, one can reveal that despite the apparent differences between the two Hamiltonians, the decompositions of the coherence are in fact similar. This illustrates the utility of our approach where coherence can be used to characterize a state to reveal hidden similarities between different systems.

We note that several other works have examined quantum coherence experimentally recently [24–27]. A coherence witness was introduced in Ref. [24] to detect the total coherence through a violation of Leggett-Garg type inequality [28]. Meanwhile the amount of coherence in a single photonic qubit was measured experimentally [25] using the robustness of coherence [13]. These works studied coherence in unipartite systems and did not analyze the coherence decompositions, their distribution and the consequent trade-off relations in multipartite systems.

Description of the quantum system.— We experimentally study tripartite quantum systems realized with nuclear spin qubits in this work. Diethyl fluoromalonate molecules are used to perform the target adiabatic evolution via a Trotter decomposition. A complete description of the experimental set up and procedure is given in the Supplementary Materials. In this work, we study two different tripartite quantum systems. The first system is

an Ising model described by the Hamiltonian

$$H_{zz}(t) = \omega_z \sum_{i=1,2,3} S_i^z + \omega_x \sum_{i=1,2,3} S_i^x + 2J_2(t) \sum_{1 \leq i < j \leq 3} S_i^z S_j^z, \quad (1)$$

where $S_i^{z/x}$ is the nuclear spin in the z/x -direction and J_2 represents the two-body interaction strength with $\omega_z = -2$ being the magnetic field in the longitudinal direction. A small transverse field $\omega_x = 0.1$ is provided to lift the degeneracy of the ground state so that the adiabatic evolution is possible. Initially when we set $J_2 = 0$ and $\omega_x \ll \omega_z$, the ground state is nearly a separable state $|000\rangle$. The state is adiabatically evolved by increasing J_2 from 0 to $|\omega_z|$ in order to obtain a state close to $|W\rangle = (|001\rangle + |010\rangle + |100\rangle)/\sqrt{3}$ at the end of the evolution [29]. The fidelity between the final ground state and $|W\rangle$ is 0.9978 while our experimental final state has a fidelity to $|W\rangle$ as high as 0.9578.

The second quantum system we consider has the following form:

$$H_{zzz}(t) = \omega_x \sum_{i=1,2,3} S_i^x + 4J_3(t) S_1^z S_2^z S_3^z, \quad (2)$$

where J_3 is the three-body interaction strength which varies from 0 to 5 during the adiabatic evolution. The corresponding initial and final ground states are $|---\rangle$ and, in the sense of zero-order perturbation, $|G\rangle = (|001\rangle + |010\rangle + |100\rangle + |111\rangle)/2$, respectively. The fidelity between the final ground state and $|G\rangle$ is 0.9996 while our experimental final state has a fidelity to $|G\rangle$ as high as 0.9661. The final state has both bipartite and tripartite coherences. For both the quantum systems, the coherence is measured at each stage of the evolution using quantum tomography methods (see Supplementary Materials).

Quantifying coherence.— To measure coherence we use the square root of quantum version of the Jensen-Shannon divergence (QJSD) [30–33]

$$\mathcal{D}(\rho, \sigma) = \sqrt{\frac{1}{2} [\mathcal{S}_r(\rho \| (\rho + \sigma)/2) + \mathcal{S}_r(\sigma \| (\rho + \sigma)/2)]}. \quad (3)$$

Here ρ and σ are two density matrices of the same dimensionality and $\mathcal{S}_r(\rho_1 \| \rho_2) = \text{tr} \rho_1 \log(\rho_1 / \rho_2)$ is the quantum relative entropy. Using this measure, the total coherence in the system is

$$C_T(\rho) \equiv \mathcal{D}(\rho, \rho_d), \quad (4)$$

where ρ is the density matrix and $\rho_d = \sum_k \langle k | \rho | k \rangle |k\rangle \langle k|$ is the diagonal density matrix with $|k\rangle$ representing the eigenstates of S_j^z . The global and local coherence are defined respectively as [12]

$$C_G(\rho) \equiv \mathcal{D}(\rho, \pi(\rho)); \quad C_L \equiv \mathcal{D}(\pi(\rho), [\pi(\rho)]_d). \quad (5)$$

Here $\pi(\rho) \equiv \otimes_i \rho_i$, where $\rho_i = \text{tr}_{\nu \neq i} \rho$ and footnotes i, j are indices of subsystems. Footnote d indicates the diagonal part of the density matrix in the S^z -basis. In terms

of the coherence trade-off, the more relevant quantity is the absolute coherence defined as

$$\mathcal{C}_A(\rho) \equiv \mathcal{D}(\rho, [\pi(\rho)]_d), \quad (6)$$

which is different from the total coherence \mathcal{C}_T and is the total amount of coherence in the product basis. The reference state $[\pi(\rho)]_d$ for absolute coherence contains neither coherence or correlations between the subsystems, while the reference state for total coherence ρ_d can potentially contain classical correlations. Since our measure $\mathcal{D}(\rho, \sigma)$ satisfies the triangle inequality for a multipartite system up to five qubits according to numerical studies [34], we have the trade-off relation (see Fig. 1(b))

$$\mathcal{C}_A \leq \mathcal{C}_L + \mathcal{C}_G. \quad (7)$$

The total coherence \mathcal{C}_T does not satisfy this trade-off relation since the reference state $\pi(\rho)$ is used.

One of the interesting aspects of tripartite systems is that coherence can be distributed in different ways. It is well-known that for entanglement, GHZ and W states are two different classes of tripartite entangled states [35]. The entanglement in a GHZ state is genuinely tripartite, whereas in a W state, the entanglement is bipartite in nature. In this context, it is interesting to examine the coherence additionally in a bipartite fashion. To this end, we evaluate the coherence between qubit 1 and the bipartite block 23

$$\mathcal{C}_{1:23} \equiv \mathcal{D}(\rho, \rho_1 \otimes \rho_{23}), \quad \mathcal{C}_{2:3} \equiv \mathcal{D}(\rho_{23}, \rho_2 \otimes \rho_3). \quad (8)$$

Here $\mathcal{C}_{1:23}$ measures the coherence between qubit 1 and the bipartite block 23 and $\mathcal{C}_{2:3}$ is the coherence in the bipartite block 23. We note that including ρ_1 does not make any difference to the global coherence, and $\mathcal{C}_{2:3} = \mathcal{D}(\rho_1 \otimes \rho_{23}, \pi(\rho))$; the proof is given in the Supplementary Materials. Complementary to the coherence $\mathcal{C}_{1:23}$ we have the contribution

$$\mathcal{C}_A^{1:23} \equiv \mathcal{D}(\rho_1 \otimes \rho_{23}, [\pi(\rho)]_d). \quad (9)$$

Based on these coherence distributions we have the following trade-off relations

$$\mathcal{C}_A \leq \mathcal{C}_{1:23} + \mathcal{C}_A^{1:23}; \quad \mathcal{C}_A^{1:23} \leq \mathcal{C}_{2:3} + \mathcal{C}_L. \quad (10)$$

Since $\mathcal{C}_{1:23}$ and $\mathcal{C}_{2:3}$ are global coherences, they give another trade-off relation

$$\mathcal{C}_G \leq \mathcal{C}_{1:23} + \mathcal{C}_{2:3}. \quad (11)$$

The four equations in (7), (10) and (11) correspond to the four triangles that are present in Fig. 1(b). They are also four trade-off relations that can be verified for the generated tripartite states.

Coherence trade-off. – The variation of the coherence contributions during the evolution is shown in Fig. 2. For Hamiltonian H_{zz} , at $J_2 = 0$, the interactions are turned

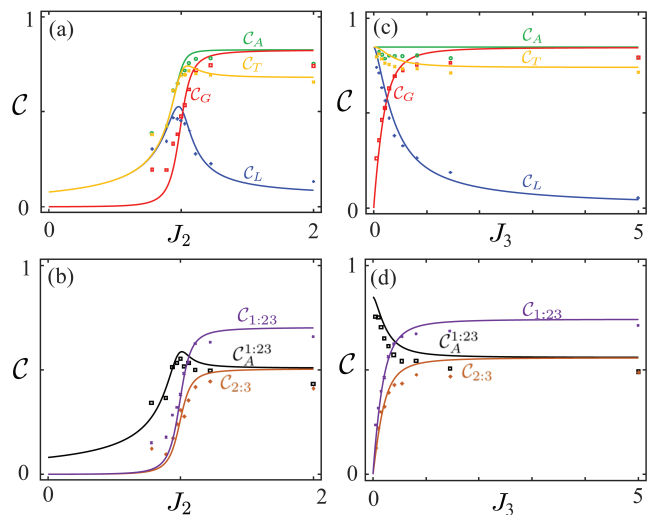


FIG. 2. The variation of different coherences as shown for the Hamiltonians (a),(b) H_{zz} and (c),(d) H_{zzz} , as a function of the interaction parameters. The experimental data is shown by the points and the lines show the theoretically obtained results.

off and the ground state is a product state. It is locally rotated from the state $|000\rangle$ ($\mathcal{C}_L = \mathcal{C}_G = 0$), due to the transverse field ω_x which induces a small local coherence. We observe that there are two regions, $J_2 \in [0, 1]$ with \mathcal{C}_L and \mathcal{C}_G increasing and $J_2 \in [1, 2]$ with \mathcal{C}_L decreasing and \mathcal{C}_G increasing. The crossover at $J_2 = 1$ corresponds to a quantum phase transition in a spin system with two-body interactions [29]. For the Hamiltonian H_{zzz} , at $J_3 = 0$, the ground state is $|---\rangle$, a coherent product state and hence $\mathcal{C}_G = 0$ and \mathcal{C}_L is maximal. At $J_3 = 5$, the ground state is nearly $|G\rangle$ for which $\mathcal{C}_L = 0$ and \mathcal{C}_G is maximal. The two distinct regions of H_{zzz} are $J_3 \in [0, 0.25]$ ($\mathcal{C}_L > \mathcal{C}_G$) and $J_3 \in [0.25, 5]$ ($\mathcal{C}_L < \mathcal{C}_G$) with the crossover at $J_3 = 0.25$. They are related to a critical point at $J_3 = \omega_x$ for a spin system with three-body interaction in the thermal dynamic limit [29, 36–41]. We note that there are regions where $\mathcal{C}_G > \mathcal{C}_T$ for both H_{zz} and H_{zzz} . This is due to our definition of global coherence, where all correlations between the qubits are broken by forming a product state, whereas in the definition of total coherence, classical correlations can be present in the decohered state. This verifies that \mathcal{C}_A is the more appropriate quantity in the context of trade-off relations.

To visualize the expected trade-off relations according to (4), (7) and (11), we look at the ratios $\mathcal{C}_G/\mathcal{C}_L$, $\mathcal{C}_{2:3}/\mathcal{C}_L$, $\mathcal{C}_{1:23}/\mathcal{C}_A^{1:23}$ and $\mathcal{C}_{2:3}/\mathcal{C}_{1:23}$ using both experimental data and the corresponding theoretical results as shown in Fig. 3. We observe three types of trade-off behavior corresponding to complete, partial and no trade-off. For ratios of \mathcal{C}_G and $\mathcal{C}_{2:3}$ to \mathcal{C}_L , there is a complete trade-off between these quantities, since there is a complete ex-

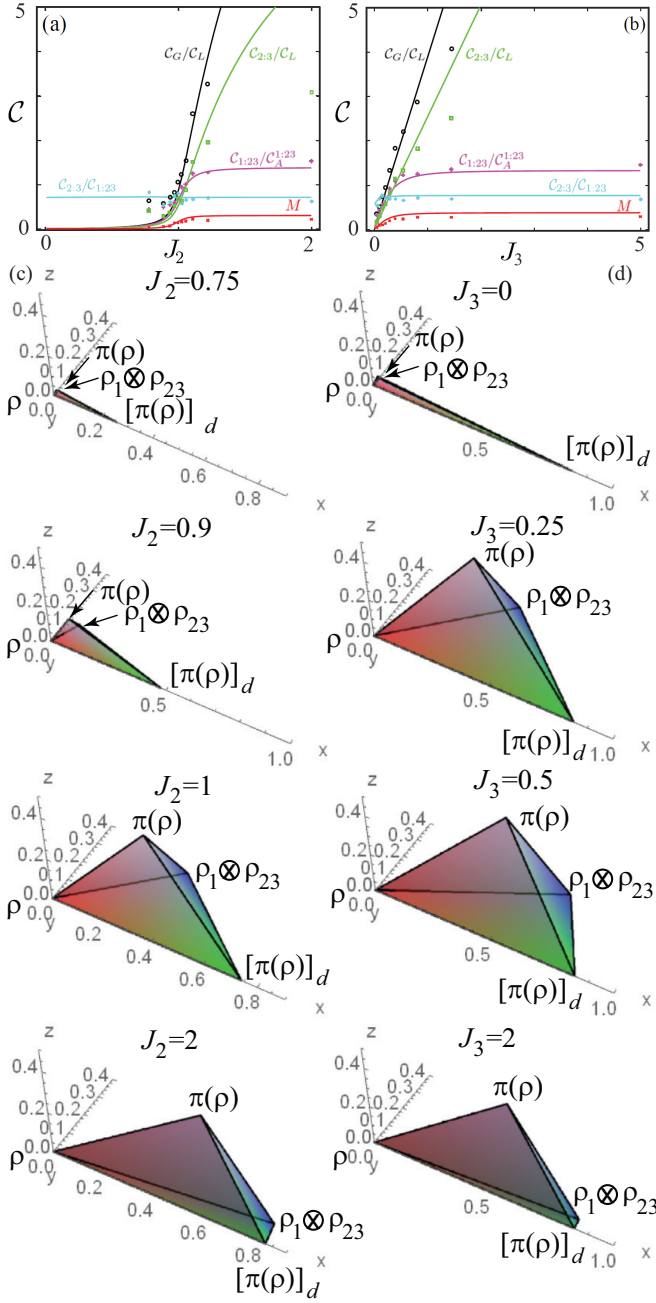


FIG. 3. The ratio between the different pairs of coherences and monogamy of coherence are shown in (a) Hamiltonian H_{zz} and (b) Hamiltonian H_{zzz} as a function of interaction parameters. The points represent the experimental data and the solid lines correspond to the theoretical calculation. (c),(d) Geometric plots of the coherence in three dimensional Euclidean space for the H_{zz} and H_{zzz} respectively, for the values of interaction parameters as marked (top to bottom). The lengths of the edges are taken to be the coherence contributions as shown in Fig. 1(b). The coordinates of the state ρ is $(0, 0, 0)$; $[\pi(\rho)]_d$ is $(C_A, 0, 0)$; $\pi(\rho)$ is $(C_G \cos \theta, C_G \sin \theta, 0)$; $\rho_1 \otimes \rho_{12}$ is $(C_{1:23} \cos \phi, C_{1:23} \sin \phi \cos \xi, C_{1:23} \sin \phi \sin \xi)$, where the angles are chosen to match the coherences as in Fig. 1(b).

change from locally to collectively distributed coherence.

Meanwhile the comparison of $C_{2:3}$ and $C_A^{1:23}$ to $C_{1:23}$ only results in a partial trade-off, where the ratios saturate to a finite value. In these cases, since both quantities in the ratio are types of global coherence, the ratios saturate to these particular values decided by large J_2, J_3 . For Hamiltonian H_{zz} , the ratio $C_{2:3}/C_{1:23}$ remains constant throughout. We attribute this to the fact that for this Hamiltonian, there is a complete qubit symmetry, such that the entangled component of the state is always of the form of a W-state. Hence when comparing two types of correlation-type coherences, although the amount of coherence both become small as $J_2 \rightarrow 0$, their ratio remains the same.

The different kinds of coherences can also be visualized geometrically as shown in Fig. 3(c),(d). Here, we plot the various coherences by assigning them Euclidean distances in three dimensional space. From the results we find that while H_{zz} and H_{zzz} have different kinds of interactions, their coherence distributions evolve similarly. The general behavior is that the states $\pi(\rho)$ and $\rho_1 \otimes \rho_{12}$ start in the vicinity of ρ , then eventually move to a location near $[\pi(\rho)]_d$, along different trajectories. The primary difference between the two Hamiltonians is that H_{zzz} always has a constant C_A , hence the size of the tetrahedron is of the same order, whereas for H_{zz} the tetrahedron starts from a point. However, apart from the overall magnitude of the coherence, the distribution of coherences are remarkably similar for both cases.

Monogamy of Coherence.— The monogamy of coherence describes the trade-off between the bipartite and tripartite global coherences of a three-body quantum system [12]. We can quantify the monogamy according to $M = C_{1:2} + C_{1:3} - C_{1:23}$, where $M > 0$ corresponds to a polygamous system and $M \leq 0$ to a monogamous system. The monogamy of coherence for the two Hamiltonians are shown in Fig. 3(a),(b). We find that the quantum systems are polygamous for every value of the interaction parameter except for the the initial value $J_2, J_3 = 0$. This points to the fact that for both the quantum systems, the most dominant form of global coherence is the bipartite global coherence. Since the coherences $C_{1:23}$ and $C_{2:3}$ are global coherences, it is only natural that they are related to C_G , the total global coherence as explained in (11). This confirms the picture provided by Fig. 3(c),(d), that the coherence generated in the two Hamiltonians is of the same type. This arises fundamentally because of the similar nature of the $|W\rangle$ and $|G\rangle$ state, which both have an bipartite-like entanglement structure.

Conclusions.— We extended the notion of coherence trade-offs introduced in Ref. [12] and experimentally studied all the trade-offs that are possible with the four point decompositions as shown in Fig. 1(b). Each point in the diagram corresponds to removing a coherence contribution. For example, the state $\pi(\rho)$ removes all the inter-qubit coherence and the state $[\pi(\rho)]_d$ removes all the coherence including that lying within the qubits.

Since we are dealing with a tripartite system, we further performed a bipartite decomposition where the coherence between the site 1 and bipartite block 23 is removed. Our results point to the fact that the trade-off relations are generic behavior and are always obeyed as we move from a separable state to an entangled state. The trade-off behavior is also consistent with approaches where coherence is considered a resource, and coherence is converted into different forms [42], which may have different sensitivities to decoherence [19, 43]. We also examined the distribution of global coherence using the property of monogamy of coherence and it was found that both the states were polygamous except when the interactions were turned off. The characterization of a quantum system through the coherence distribution diagrams in Fig. 3(c),(d) was shown to be an effective tool to visualize the quantum state. It is interesting to note that while H_{zz} and H_{zzz} have different types of interactions and different initial states, the final quantum states have similar quantum properties. Hence, using the coherence decompositions and the trade-off relations, one can gain insight into the essential character of a given state, which may not be obvious simply by examining the wavefunction.

The researchers at USTC are supported by the National Key Research and Development Program of China (Grants No. 2018YFA0306600 and 2016YFA0502400), the National Natural Science Foundation of China (Grants No. 81788101, 91636217, 11722544, 11761131011, and 31971156), the CAS (Grants No. GJJSTD20200001, QYZDY-SSW-SLH004 and YIPA 2015370), the Anhui Initiative in Quantum Information Technologies (Grant No. AHY050000), the National Youth Talent Support Program. TB and RC are supported by the Shanghai Research Challenge Fund; New York University Global Seed Grants for Collaborative Research; National Natural Science Foundation of China (61571301, D1210036A); the NSFC Research Fund for International Young Scientists (11650110425, 11850410426); NYU-ECNU Institute of Physics at NYU Shanghai; the Science and Technology Commission of Shanghai Municipality (17ZR1443600); the China Science and Technology Exchange Center (NGA-16-001); and the NSFC-RFBR Collaborative grant (81811530112).

* These authors contributed equally to this work.

† tim.byrnes@nyu.edu

‡ fzshi@ustc.edu.cn

§ djf@ustc.edu.cn

- [1] R. J. Glauber, *Physical Review* **131**, 2766 (1963).
- [2] E. Sudarshan, *Physical Review Letters* **10**, 277 (1963).
- [3] M. O. Scully and M. S. Zubairy, *Quantum optics* (1999).
- [4] T. Baumgratz, M. Cramer, and M. Plenio, *Physical Review Letters* **113**, 140401 (2014).
- [5] Z.-H. Ma, J. Cui, Z. Cao, S.-M. Fei, V. Vedral, T. Byrnes, and C. Radhakrishnan, *EPL (Europhysics Letters)* **125**, 50005 (2019).
- [6] G. Adesso, T. R. Bromley, and M. Cianciaruso, *Journal of Physics A: Mathematical and Theoretical* **49**, 473001 (2016).
- [7] A. Winter and D. Yang, *Physical Review Letters* **116**, 120404 (2016).
- [8] E. Chitambar and G. Gour, *Physical Review Letters* **117**, 030401 (2016).
- [9] A. Streltsov, G. Adesso, and M. B. Plenio, *Reviews of Modern Physics* **89**, 041003 (2017).
- [10] A. Streltsov, S. Rana, P. Boes, and J. Eisert, *Physical Review Letters* **119**, 140402 (2017).
- [11] L.-H. Shao, Z. Xi, H. Fan, and Y. Li, *Physical Review A* **91**, 042120 (2015).
- [12] C. Radhakrishnan, M. Parthasarathy, S. Jambulingam, and T. Byrnes, *Physical Review Letters* **116**, 150504 (2016).
- [13] C. Napoli, T. R. Bromley, M. Cianciaruso, M. Piani, N. Johnston, and G. Adesso, *Physical Review Letters* **116**, 150502 (2016).
- [14] D. Girolami, *Physical Review Letters* **113**, 170401 (2014).
- [15] C. Radhakrishnan, Z. Ding, F. Shi, J. Du, and T. Byrnes, *Annals of Physics* **409**, 167906 (2019), ISSN 0003-4916.
- [16] A. Streltsov, E. Chitambar, S. Rana, M. Bera, A. Winter, and M. Lewenstein, *Physical Review Letters* **116**, 240405 (2016).
- [17] G. Karpat, B. Çakmak, and F. Fanchini, *Physical Review B* **90**, 104431 (2014).
- [18] C. Radhakrishnan, I. Ermakov, and T. Byrnes, *Physical Review A* **96**, 012341 (2017).
- [19] C. Radhakrishnan, M. Parthasarathy, S. Jambulingam, and T. Byrnes, *Scientific Reports* **7**, 13865 (2017).
- [20] V. Coffman, J. Kundu, and W. K. Wootters, *Physical Review A* **61**, 052306 (2000).
- [21] M. Koashi and A. Winter, *Physical Review A* **69**, 022309 (2004).
- [22] G. L. Giorgi, *Physical Review A* **84**, 054301 (2011).
- [23] R. Prabhu, A. K. Pati, A. Sen, U. Sen, et al., *Physical Review A* **85**, 040102 (2012).
- [24] Z.-Q. Zhou, S. F. Huelga, C.-F. Li, and G.-C. Guo, *Physical Review Letters* **115**, 113002 (2015).
- [25] Y.-T. Wang, J.-S. Tang, Z.-Y. Wei, S. Yu, Z.-J. Ke, X.-Y. Xu, C.-F. Li, and G.-C. Guo, *Physical Review Letters* **118**, 020403 (2017).
- [26] K.-D. Wu, T. Theurer, G.-Y. Xiang, C.-F. Li, G.-C. Guo, M. B. Plenio, and A. Streltsov, *npj Quantum Information* **6**, 1 (2020).
- [27] Y. Yuan, Z. Hou, J.-F. Tang, A. Streltsov, G.-Y. Xiang, C.-F. Li, and G.-C. Guo, *npj Quantum Information* **6**, 1 (2020).
- [28] A. J. Leggett, *Reports on Progress in Physics* **71**, 022001 (2008).
- [29] X. Peng, J. Zhang, J. Du, and D. Suter, *Physical Review A* **81**, 042327 (2010).
- [30] J. Lin, *IEEE Transactions on Information theory* **37**, 145 (1991).
- [31] J. Briët and P. Harremoës, *Physical Review A* **79**, 052311 (2009).
- [32] A. Majtey, P. Lamberti, and D. Prato, *Physical Review A* **72**, 052310 (2005).
- [33] P. Lamberti, A. Majtey, A. Borrás, M. Casas, and

- A. Plastino, *Physical Review A* **77**, 052311 (2008).
- [34] P. W. Lambert, A. P. Majtey, A. Borrás, M. Casas, and A. Plastino, *Physical Review A* **77**, 052311 (2008).
- [35] W. Dür, G. Vidal, and J. I. Cirac, *Physical Review A* **62**, 062314 (2000).
- [36] F. Igloi, *Journal of Physics A: Mathematical and General* **20**, 5319 (1987), ISSN 0305-4470.
- [37] K. A. Penson, J. M. Debierre, and L. Turban, *Physical Review B* **37**, 7884 (1988).
- [38] K. A. Penson, R. Jullien, and P. Pfeuty, *Physical Review B* **26**, 6334 (1982).
- [39] F. Igloi, D. V. Kapor, M. Skrinjar, and J. Solyom, *Journal of Physics A: Mathematical and General* **16**, 4067 (1983), ISSN 0305-4470.
- [40] R. J. Baxter and F. Y. Wu, *Physical Review Letters* **31**, 1294 (1973).
- [41] J. K. Pachos and M. B. Plenio, *Physical Review Letters* **93**, 056402 (2004).
- [42] K.-D. Wu, Z. Hou, Y.-Y. Zhao, G.-Y. Xiang, C.-F. Li, G.-C. Guo, J. Ma, Q.-Y. He, J. Thompson, and M. Gu, *Physical review letters* **121**, 050401 (2018).
- [43] H. Cao, C. Radhakrishnan, M. Su, M. M. Ali, C. Zhang, Y.-F. Huang, T. Byrnes, C.-F. Li, and G.-C. Guo, *Phys. Rev. A* **102**, 012403 (2020).

Experimental study of quantum coherence decomposition and trade-off relations in a tripartite system: supplementary material

Zhe Ding,^{1,2,*} Ran Liu,^{1,2,*} Chandrashekar Radhakrishnan,^{3,4,5,*} Wenchao Ma,⁶ Xinhua Peng,^{1,2,7} Ya Wang,^{2,7} Tim Byrnes,^{8,9,5,10,11,†} Fazhan Shi,^{1,2,7,‡} and Jiangfeng Du^{1,2,7,§}

¹Hefei National Laboratory for Physical Sciences at the Microscale and Department of Modern Physics, University of Science and Technology of China, Hefei, 230026, China

²CAS Key Laboratory of Microscale Magnetic Resonance, University of Science and Technology of China, Hefei, 230026, China

³Laboratoire ESIEA Numérique et Société, ESIEA, 9 Rue Vesale, Paris 75005, France

⁴New York University, 1555 Century Avenue, Pudong, Shanghai 200122, China

⁵NYU-ECNU Institute of Physics at NYU Shanghai, 3663 Zhongshan Road North, Shanghai 200062, China

⁶Department of Chemistry, Massachusetts Institute of Technology, Cambridge, Massachusetts 02139, USA

⁷Synergetic Innovation Center of Quantum Information and Quantum Physics, University of Science and Technology of China, Hefei, 230026, China

⁸New York University Shanghai, 1555 Century Ave, Pudong, Shanghai 200122, China

⁹State Key Laboratory of Precision Spectroscopy, School of Physical and Material Sciences, East China Normal University, Shanghai 200062, China

¹⁰National Institute of Informatics, 2-1-2 Hitotsubashi, Chiyoda-ku, Tokyo 101-8430, Japan

¹¹Department of Physics, New York University, New York, NY 10003, USA

PROOF OF $C_{(1)2:3} = C_{2:3}$

One of the important distributions of quantum coherence is $C_{1:23}$ which is the coherence between the qubit 1 and the bipartite block 23. A complementary distribution is $C_{(1)2:3}$ which is the global coherence in the $\rho_1 \otimes \rho_{23}$ system. Below we prove that for the QJSD-based measure of quantum coherence $C_{(1)2:3} = C_{2:3}$.

Theorem 1. $C_{(1)2:3}$ is equal to the global coherence $C_{2:3}$ in the system.

Proof. The coherence $C_{(1)2:3}$ in terms of the QJSD based coherence measure is

$$C_{(1)2:3} = \sqrt{\mathcal{J}(\rho_1 \otimes \rho_{23}, \rho_1 \otimes \rho_2 \otimes \rho_3)}. \quad (\text{S1})$$

For two independent quantum systems ρ and σ , the additivity of the von Neumann entropy leads to

$$\mathcal{S}(\rho \otimes \sigma) = \mathcal{S}(\rho) + \mathcal{S}(\sigma). \quad (\text{S2})$$

Due to this additivity, the QJSD obeys the restricted additivity [1] as given below:

$$\mathcal{J}(\rho \otimes \sigma_1, \rho \otimes \sigma_2) = \mathcal{J}(\sigma_1, \sigma_2), \quad (\text{S3})$$

and so consequently we find that

$$C_{(1)2:3} = \sqrt{\mathcal{J}(\rho_{23}, \rho_2 \otimes \rho_3)} = C_{2:3}. \quad (\text{S4})$$

□

ANALYSIS OF GROUND STATES

In this work, we investigate two different tripartite quantum systems by adiabatically evolving them. In the

first quantum system we have only two-body interactions and the Hamiltonian of the system reads:

$$H_{zz}(t) = \omega_z \sum_{i=1,2,3} S_i^z + \omega_x \sum_{i=1,2,3} S_i^x + 2J_2(t) \sum_{1 \leq i < j \leq 3} S_i^z S_j^z. \quad (\text{S5})$$

The Hamiltonian of the second quantum system with three-body interactions is

$$H_{zzz}(t) = \omega_x \sum_{i=1,2,3} S_i^x + 4J_3(t) S_1^z S_2^z S_3^z. \quad (\text{S6})$$

For the Hamiltonian H_{zz} , during the experiment, we assume $\omega_z = -2$, $\omega_x = 0.1 \ll |\omega_z|$ and vary J_2 from 0 to 2. The Hamiltonian is symmetric under permutation of spins. When there is no perturbation, that is when $\omega_x = 0, J_2 = 0$, the ground state is $|000\rangle$. We analyze the quantum state under the symmetric basis $\{|000\rangle, |W_{001}\rangle, |W_{110}\rangle, |111\rangle\}$ where

$$\begin{aligned} |W_{001}\rangle &= (|001\rangle + |010\rangle + |100\rangle)/\sqrt{3}, \\ |W_{110}\rangle &= (|110\rangle + |101\rangle + |011\rangle)/\sqrt{3}. \end{aligned}$$

The ground states are analyzed using perturbation theory. Defining $H_0 = \omega_z \sum_{i=1,2,3} S_i^z + 2J_2(t) \sum_{1 \leq i < j \leq 3} S_i^z S_j^z$ and $V = \omega_x \sum_{i=1,2,3} S_i^x$ where V is the perturbation term. The initial ground state under zero order perturbation is $|000\rangle$. At the end of the evolution, $\omega_z, J_2 \gg \omega_x$ under zero perturbation, the ground state is $|W\rangle_{001}$. The corresponding energy level diagram is shown in Fig. S1 (a). To compare the fidelity of the experimental state at $J_2 = 2$, we can calculate the ground

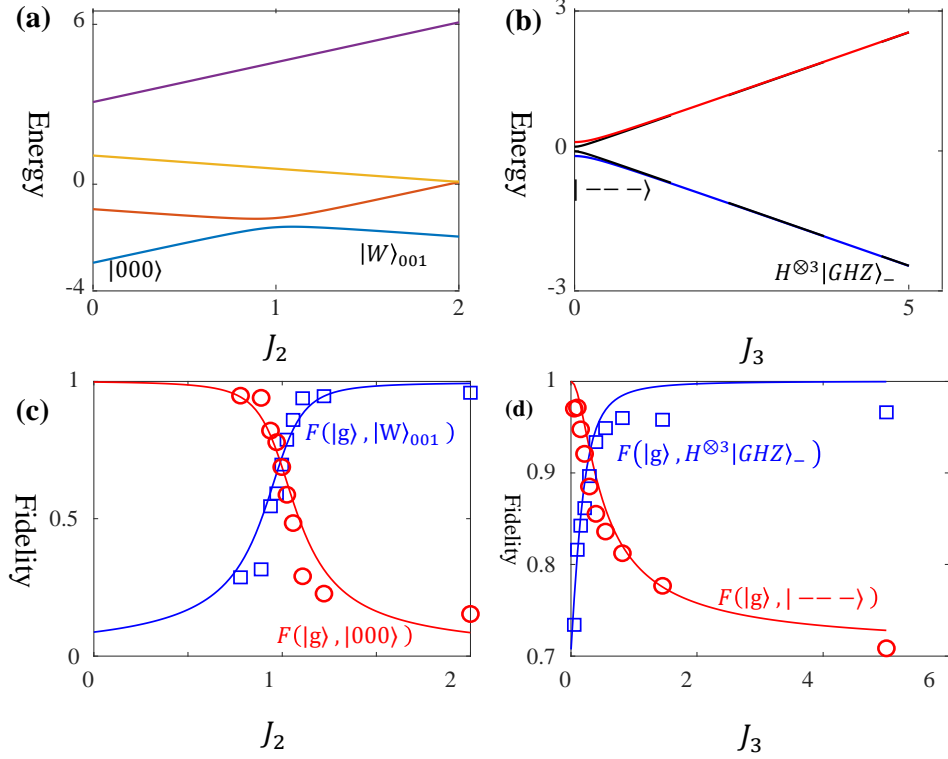


FIG. S1. (a, b) The energy levels. (c, d) The fidelity between ground states and goal states. The solid lines show the numerical results. The circles and squares show the experiment results.

state up to the first order perturbation[2]

$$\begin{aligned}
 |g\rangle &\approx |g^{(0)}\rangle + \sum_{k \neq g} \frac{V_{kg}}{E_g^{(0)} - E_k^{(0)}} |k^{(0)}\rangle \\
 &= |g^{(0)}\rangle + \frac{\omega_x}{\omega_z} |W\rangle_{110} - \frac{\sqrt{3}}{2} \frac{\omega_x}{2J_2 + \omega_z} |000\rangle \quad (S7)
 \end{aligned}$$

Here, $|g^{(0)}\rangle = |W\rangle_{001}$ is the zeroth order approximation of the ground state. The fidelity between $|W\rangle_{001}$ and final ground state in the sense of first order perturbation is :

$$F(|g\rangle, |W\rangle_{001}) \approx 1 / \left(1 + \left(\frac{\omega_x}{\omega_z} \right)^2 + \left(\frac{\sqrt{3}}{2} \frac{\omega_x}{2J_2 + \omega_z} \right)^2 \right) \quad (S8)$$

We also numerically diagonalize the Hamiltonian directly and calculate the fidelities. In Fig. S1(c), we show the numerically calculated fidelities $F(|g\rangle, |W\rangle_{001})$ through a blue solid line and the experimental data fidelities through blue squares. From the figure, we can see that the numerically calculated final fidelity is 0.9978 and the experimental fidelity is as high as 0.9578.

Next, we analyze the ground state of Hamiltonian H_{zzz} . The initial Hamiltonian $J_3 = 0$ is $H_{zzz}(0) = \omega_x \sum_{i=1,2,3} S_i^x$ and the initial ground state is $|---\rangle$,

where $|-\rangle = (|0\rangle - |1\rangle)/\sqrt{2}$. At the end of the adiabatic evolution the final Hamiltonian is obtained when $J_3 = 5$. For the final Hamiltonian $J_3 \gg \omega_x$, the unperturbed part of the Hamiltonian is $H_0 = 4J_3(t)S_1^z S_2^z S_3^z$ and the perturbation term is $V = \omega_x \sum_{i=1,2,3} S_i^x$. The states $|W\rangle_{001}$ and $|111\rangle$ expands a degenerated ground state subspace in the non-perturbed Hamiltonian. Since the transition term between these two states in H_{zzz} is zero, we need to use first-order perturbation theory, in which the projection of the approximated ground state to the degenerate subspace is the solution to the secular equation:

$$\sum_{\nu \in g} c_{g\nu} \left(\sum_{n \notin g} \frac{V_{g\nu, n} V_{n, g\nu}}{E_g^{(0)} - E_n^{(0)}} - \delta_{\mu\nu} \Delta E_g \right) = 0 \quad (S9)$$

In the above equation, ΔE_g is the perturbation of the ground state's energy, g represents the degenerate ground state subspace, μ, ν are the labels of the basis in the subspace. We label $|W\rangle_{001}$ and $|111\rangle$ as $g1$ and $g2$ respectively. By solving Eq. (S9), we find:

$$\begin{aligned}
 |g\rangle &\approx \frac{\sqrt{3}}{2} |W\rangle_{001} + \frac{1}{2} |111\rangle \\
 &= H^{\otimes 3} |GHZ\rangle_- \\
 &= |G\rangle \quad (S10)
 \end{aligned}$$

The energy levels of this evolution are plotted in Fig. S1(b). To estimate the final state, we calculate the first order perturbation of the ground state and include the contribution from the other two energy levels.

$$\begin{aligned} |g\rangle &\approx |G\rangle + \sum_{n \notin g} \sum_{\mu} \frac{V_{n,g\mu} c_{g\mu}}{E_g^{(0)} - E_n^{(0)}} |n^{(0)}\rangle \\ &= |G\rangle - \frac{\omega_x}{J_3} \left(\frac{3}{4} |000\rangle + \frac{3\sqrt{3}}{4} |W\rangle_{110} \right) \end{aligned} \quad (\text{S11})$$

Using this we can estimate the final state's fidelity,

$$F(|g\rangle, |G\rangle) \approx 1 / \left(1 + \left(\frac{3\omega_x}{2J_3} \right)^2 \right) \quad (\text{S12})$$

We also numerically diagonalize the Hamiltonian directly and calculate the fidelities. The numerically calculated value of the fidelity is shown through blue lines in Fig. S1(d), and the fidelity of the final state is 0.9996. The fidelities of experimental data are displayed as blue squares among which the final fidelity is 0.9661.

The tomography of the experimental states is shown through Fig. (S2) (a) and (b) for the Hamiltonians H_{zz} and H_{zzz} respectively and in Fig. (S2) (c) the corresponding basis is shown for reference. In Fig. S2 (d) and (e) we display the fidelities between the experimental states and the corresponding ground states.

EXPERIMENTAL PROTOCOL

In the experiment, we use diethyl fluoromalonate molecules dissolved in ^2H -labeled chloroform as the three-qubit spin system. The molecular structure of diethyl fluoromalonate is shown in Fig. S3 (a). The three nuclear spins ^{13}C , ^1H and ^{19}F in the molecule acts as the qubits. The natural Hamiltonian of the system is

$$H_{\text{spin}} = \sum_{i=1,2,3} 2\pi\delta_i S_i^z + \sum_{1 \leq i < j \leq 3} 2\pi J_{ij} S_i^z S_j^z \quad (\text{S13})$$

where S_i^z is the nuclear spin in the z -direction, δ_i is the chemical shift of the nuclear spin and J_{ij} is the coupling between the i -th and the j -th nucleus as given in Fig. S3 (b). The NMR experiment was carried out on a Bruker Avance III 400 MHz (9.4 T) spectrometer at 303K. In the first step of the experiment, a pseudopure state (PPS) of the form $\rho = (1 - \mu)I/8 + \mu|\psi\rangle\langle\psi|$ is prepared from thermal equilibrium state using a line-selective method[3], where $|\psi\rangle$ is an arbitrary pure state. Here the mixing parameter $\mu \approx 10^{-5}$ and I denotes the 8×8 identity matrix. The adiabatic pathway is numerically optimized to generate the desired ground state. The schematic diagram of the sequence to fulfill H_{zz} and H_{zzz} are shown in Fig. S3 (c) and (d). At each stage, the corresponding density matrices are reconstructed using tomographic techniques.

EXPERIMENTAL DETAILS OF THE REFOCUSING SCHEME

Experimentally, the adiabatic evolution is performed in discrete steps. The evolution of each segment $U_{exp}^{(k)}(t_m)$, is a Trotter expansion of the ideal one $U_{ide}^{(k)}(t_m)$, which can be expressed as

$$\begin{aligned} U_{ide}^{(k)}(t_m) &= e^{-i[H_x^{(k)} + H_z^{(k)}(t_m)]\tau^{(k)}} \\ &= e^{-iH_x^{(k)}\tau^{(k)}/2} e^{-iH_z^{(k)}(t_m)\tau^{(k)}} e^{-iH_x^{(k)}\tau^{(k)}/2} + O(\tau^3) \\ &= U_{exp}^{(k)}(t_m) + O(\tau^3) \end{aligned} \quad (\text{S14})$$

where $k \in \{1, 2\}$ labels two Hamiltonians, i.e. $H^{(1)} = H_{zz}$, $H^{(2)} = H_{zzz}$. $\tau^{(k)}$ is the interval of each step and $m \in [0, M]$ is the index of each step. We use a refocusing scheme to achieve each step in our work. In this method, tuned pulses are applied during each Trotter slice, and the Hamiltonian in each short time period is accurately controlled.

Two different quantum systems are experimentally studied in our work. In the first system, we construct a tripartite Hamiltonian with identical two-body interactions as shown in Eq. (S5). The quantum system is adiabatically evolved by tuning the two qubit interaction strength adiabatically over the range $[0, 2]$. Experimentally, the adiabatic state transfer (ASP) is performed in discrete steps, such that $J_2(t)$ assumes discrete value $J_2(t_m)$ with $m = 0, \dots, M^{(1)}$. At each time step, the evolution is generated using multipulse sequence $U_{exp}^{(1)}(t_m)$ using Trotter expansion formula as described in Eq. (S14). The resulting Hamiltonian is

$$H_x^{(1)} = \omega_x \sum_{i=1,2,3} S_i^x, \quad (\text{S15})$$

$$H_z^{(2)}(J_2(t_m)) = \omega_z \sum_{i=1,2,3} S_i^z + 2J_2(t_m) \sum_{1 \leq i < j \leq 3} S_i^z S_j^z$$

A schematic description of the refocusing scheme is shown in Fig. S3 (c) where the narrow unfilled rectangles denote $\pi/2$ pulses, and the wide ones show π pulses. By defining $d_{ij} = 1/(2J_{ij})$, the width of filled pulse in (c) are all $\omega_x\tau^{(1)}/2$ and the radio-frequency offsets for three channels are set as $FQ1_m = \omega_z/(4J_2(t_m)d_{12})$, $FQ2_m = \omega_z/(4J_2(t_m)(d_{12} + d_{13} + d_{23}))$ and $FQ3_m = \omega_z/(4J_2(t_m)d_{23})$, the delays are $\tau_m^{(1)} = \frac{J_2(t_m)\tau^{(1)}}{\pi} \times (d_{12} + d_{23})$, $\tau_m^{(2)} = \frac{J_2(t_m)\tau^{(1)}}{\pi} \times (d_{12} + d_{13})$, and $\tau_m^{(3)} = \frac{J_2(t_m)\tau^{(1)}}{\pi} \times (d_{13} + d_{23})$.

Next we consider the Hamiltonian of a tripartite quantum system with J_3 being the three-body interaction strength as shown in Eq. (S6). The interaction parameter J_3 is tuned adiabatically in the range $[0, 5]$. Again, we use a discrete refocusing scheme in which $J_3(t)$ is discretized into t_m , $m = 0, \dots, M^{(2)}$. The schematic diagram is shown in Fig. S3 (d) in which the width of the filled pulse are all $\omega_x\tau^{(2)}/2$ and the delay $d_m = \frac{J_3(t_m)\tau^{(2)}}{\pi} \times d_{12}$.

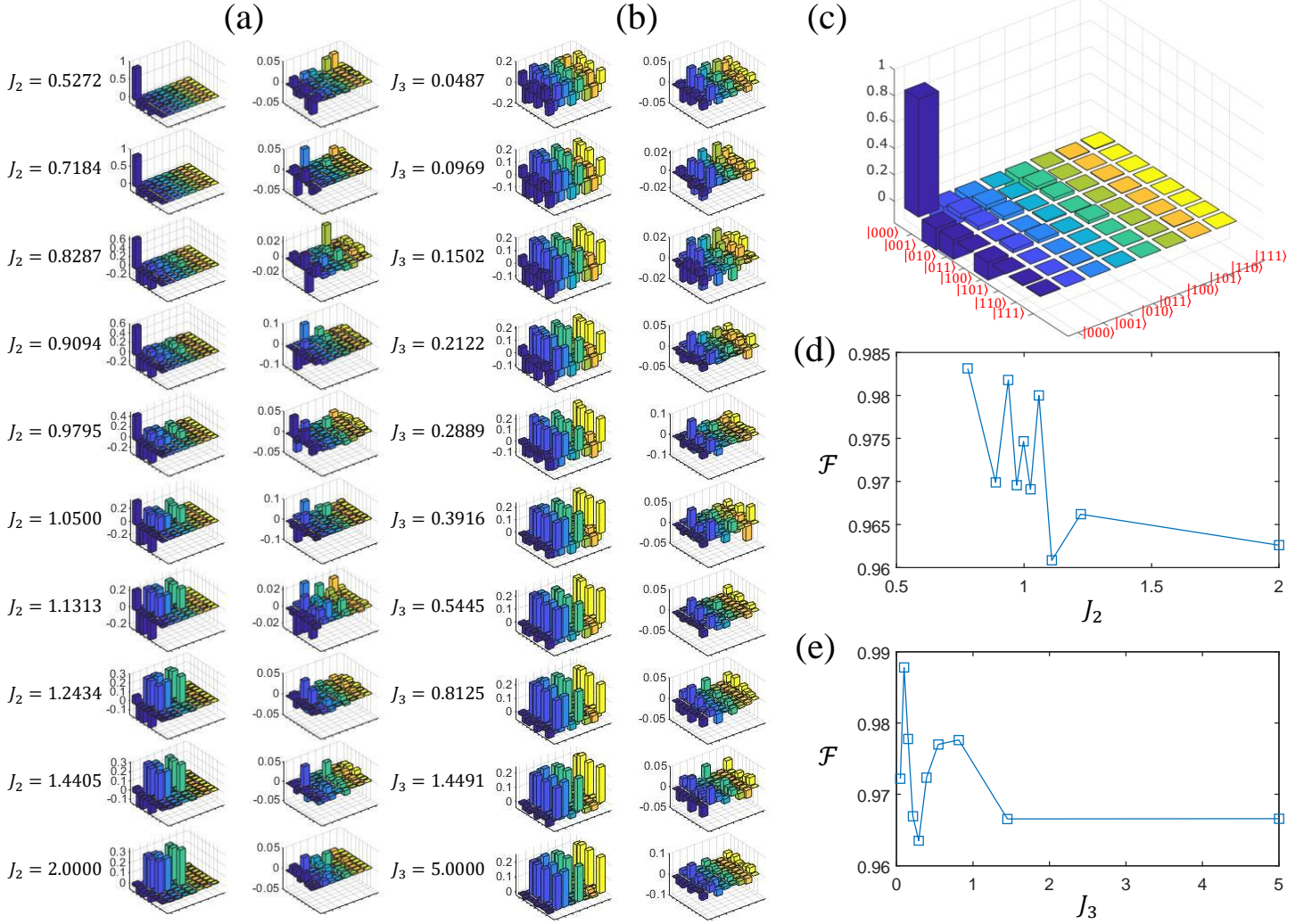


FIG. S2. Tomography results of the quantum states. (a,b) show the tomography results of all the experimental states for H_{zz} and H_{zzz} , the first columns show the real part of the density matrices while the second columns the imaginary part. (c) shows the basis of the density matrices displayed in (a,b). (d,e) show the fidelities between experimental states and ground states.

From above, one can see that the unit of studied quantities like $J_2, \omega_z, \tau^{(i)}$ always cancel out when they come into the parameters of the experiment. This means that the units of them do not matter in the experiment, only the relative relations between them matter. So, they are in arbitrary units and we don't mention the unit in the main text. We use 0.7 and 0.4 as the value of $\tau^{(1),(2)}$ when we design the experimental sequences, to see the reason why these two values are chosen, please refer to the next section.

OPTIMIZATION OF EXPERIMENTAL PARAMETERS

In the previous section, we discussed about the adiabatic evolution. As a result, τ should be kept small

enough to maintain the fidelity $U_{ide}^{(k)}(t_m)$ and $U_{exp}^{(k)}(t_m)$ high for all $m \in [0, M]$, while it should not be too small that the number of discrete steps is large. We set $\tau^{(1),(2)}$ as 0.7, 0.4, respectively, as it guarantees that $f[U_{exp}^{(k)}(t_m), U_{ide}^{(k)}(t_m)] > 99.9\%$. Here, $f(U_1, U_2)$ is the fidelity between U_1 and U_2 , which is defined as $f(U_1, U_2) = \frac{|\text{Tr}(U_1 \times U_2')|^2}{d^2}$, and d is the dimension of $U_{1,2}$. We then increase the number of steps and obtain the minimum fidelity of generated states during the adiabatic process by numerical simulation. From the adiabatic paths obtained from numerical optimization, the linear interpolation method is employed and the corresponding discrete path can then be obtained by simulation. According to the results shown in Fig.S4 (a,b), we finally set $M^{(1)} = 300$ and $M^{(2)} = 200$, respectively, to make sure the generated states are kept as close as possible to the theoretical ground states. The stepwise values of

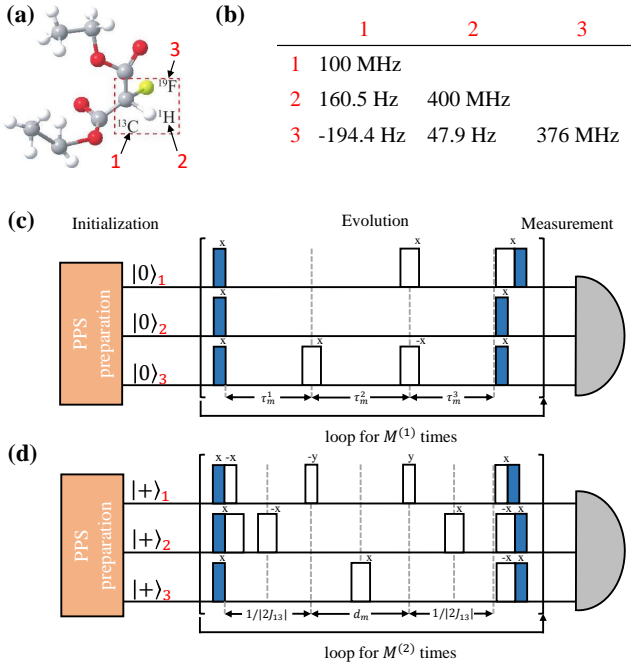


FIG. S3. a) Molecular structure of Diethyl fluoromalonate. The three nuclear spins ^{13}C , ^1H and ^{19}F adopted in the experiment are labeled. The corresponding qubit index is also marked in red for each nuclear spin with a black arrow. b) Parameters of the natural Hamiltonian of the three-spin system are shown in this table. The diagonal terms are the values of the chemical shift and the off-diagonal terms represent the scalar coupling between the different nuclei. c) and d) shows the schematic diagram explaining the experimental procedure for H_{zz} and H_{zzz} respectively. In the initialization part, we prepare the system from a pseudopure state (PPS) into the designed Hamiltonian's ground state. In the evolution part, a discrete refocusing scheme is used to perform two Hamiltonians. Combining with Trotter expansion, we can perform adiabatic evolution under any interaction. The wide and narrow unfilled pulses represent π and $\pi/2$ pulses respectively while the rotation axes are labeled above each pulse. The filled pulses represent a rotation of $\omega_x \tau/2$, where τ means the length of each Trotter slice. The measurement part is carried out using quantum state tomography.

J_2, J_3 for implementing in the experiment are shown as the discrete points in Fig.S4(c,d). Obviously, the discrete samples are denser when the gap between the two lowest energy levels decreases, and this is why the numerically optimized path can adjust speed of adiabatic transfer according to the structure of energy level and speedup the adiabatic process.

* These authors contributed equally to this work.

† tim.byrnes@nyu.edu

‡ fzshi@ustc.edu.cn

§ djf@ustc.edu.cn

- [1] A. Majtey, P. Lamberti, and D. Prato, *Physical Review A* **72**, 052310 (2005).
- [2] J. J. Sakurai and J. Napolitano, *Modern Quantum Mechanics* (Cambridge University Press, 2017), ISBN 978-1-108-42241-3.
- [3] X. Peng, X. Zhu, X. Fang, M. Feng, K. Gao, X. Yang, and M. Liu, *Chemical Physics Letters* **340**, 509 (2001).

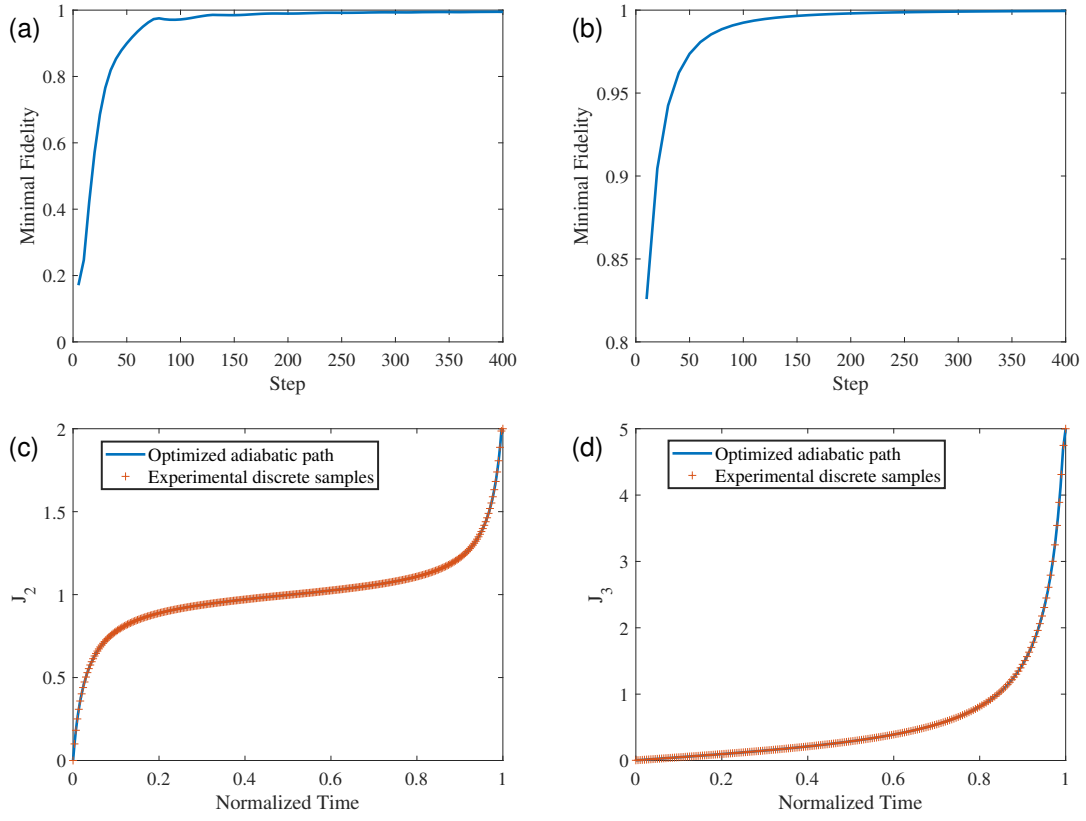


FIG. S4. (a, b) The minimum fidelity of generated states during the adiabatic process of $H^{(1),(2)}$ versus the number of steps. (c, d) The optimized adiabatic paths of $H^{(1),(2)}$ are shown as the blue solid lines, while the discrete points are sampled according to $M^{(1),(2)}$ for experimental implementing.